Journal of Manufacturing Processes 156 (2025) 611–626

Contents lists available at ScienceDirect

Journal of Manufacturing Processes

journal homepage: www.elsevier.com/locate/manpro

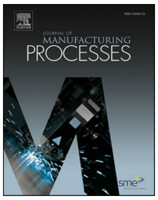

Polymer blends as a tool to improve mechanical properties and printability of metal-filled polymer filaments for material extrusion additive manufacturing in the context of sustainable manufacturing

Daria Strugova [a], S.M. Nourin Sultana [a], Jean-Philippe Leclair [a], Éric David [a], Nicole R. Demarquette [a], Vladimir Paserin [b], Lucas A. Hof [a,*]

[a] *Mechanical Engineering Department, École de technologie supérieure, Montréal, Québec, H3C 1K3, Canada*
[b] *VPM Research Inc, Missisauga, Ontario, Canada*

ARTICLE INFO

Keywords:
Material extrusion
Metal/polymer composite filaments
Thermal debinding
Sintering
Sustainable manufacturing
Polymer blends

ABSTRACT

This study reports the development and optimization of highly metal-loaded thermoplastic composite filaments for material extrusion additive manufacturing of metallic components. Nickel (Ni) and iron (Fe) powders with varying particle sizes and morphologies were combined with polyethylene (PE), polylactic acid (PLA), and PE/PLA blends as binders. The influence of particle characteristics and binder composition on filament morphology, mechanical properties, porosity, thermal behavior, and printability was systematically investigated. Composite filaments containing up to 90 wt% Ni and 80 wt% Fe were successfully extruded. Scanning electron microscopy revealed that fine Ni particles improved dispersion and reduced porosity, whereas coarse Fe particles resulted in heterogeneous packing. Thermal analyses guided debinding and sintering conditions, while mechanical testing demonstrated that PE enhanced flexibility, PLA contributed to strength, and blended systems offered a balanced compromise with good printability. Optimized 3D printing parameters enabled the fabrication of high-quality green parts, which were successfully debound and sintered using graphite powder to suppress oxidation. Dense metallic structures with controlled shrinkage and minimal residual porosity were obtained. Ni-based samples exhibited greater shrinkage and cracking due to finer particle size and higher thermal expansion. The results demonstrate a robust materials–process design strategy for FFF of metals. Unlike conventional multi-step solvent-based methods, this work employs a simple dry-mixing route and standard laboratory furnace processing without vacuum or inert atmospheres. This streamlined approach provides an environmentally friendly and scalable pathway for additive manufacturing of high-performance metallic parts.

1. Introduction

Additive manufacturing (AM), particularly material extrusion (MEX) based processes, such as Fused Deposition Modeling (FDM) or Fused Filament Fabrication (FFF), has transformed modern material fabrication by enabling rapid prototyping and the creation of intricate geometries with high design flexibility [1–3]. Thermoplastic polymers such as PLA, ABS, PETG, and TPU are commonly used due to their ease of processing and broad availability [4–7]. Recently, there has been growing interest in enhancing these polymers with functional fillers, especially metal powders, which significantly expand the material's performance capabilities [8–22]. Metal-filled polymer filaments offer a promising combination: the mechanical strength and functional properties of metals, achieved after debinding and sintering, combined with the simplicity and versatility of thermoplastic processing during 3D printing. This hybrid approach opens new possibilities for producing components in high-demand sectors such as aerospace, automotive, and biomedicine. Moreover, it offers a more energy-efficient and adaptable alternative to traditional metal manufacturing methods, such as casting, machining or powder metallurgy [23,24].

In MEX AM processes using metal-filled polymer filaments, achieving optimal performance requires a careful balance among several competing factors: high metal loading, sufficient filament flexibility, and adequate mechanical strength to enable continuous 3D printing without filament breakage. A high concentration of metal particles (between 50 and 60 vol%) is essential for producing fully dense metal parts with

---

* Corresponding author.
E-mail address: lucas.hof@etsmtl.ca (L.A. Hof).

https://doi.org/10.1016/j.jmapro.2025.11.002
Received 25 August 2025; Received in revised form 24 October 2025; Accepted 3 November 2025

Table 1
Metal-filled polymer filaments compositions used in FFF.

Feedstocks' polymers*	Metal powder	Metal loading	Characteristics	Ref.
EVA + PPC + Poly (isobutene)	Ti	0–60 vol %	- printability using FFF; - good debinding and sintering for Ti powder equal or higher larger than 50 vol%.	[18]
PLA + ATBC or PLA, + BVOH + ATBC	CuSn10	65 vol%	- significant improvements in the mechanical properties, relative density and porosity due to new formula of the binder.	[34]
TPE and grafted polyolefin	Stainless steel – 316 L	55 vol%	- fabrication fully dense metal parts (≥ 95 density) by optimizing debinding and sintering parameters.	[12]
ABS + stearic acid	Fe and Cu;	5–40 vol %	- high performance of metal/polymer filaments; - possibility of functional prototypes on the existing FDM platform.	[9]
ABS	Stainless steel – 420 SS	10–23 wt %	- improved mechanical properties as compared to the base printed polymer.	[11]
PLA	Gas atomized Ni–Cu	25–63.5 vol%	- good extrudability and windability of solution-mixed feedstock with metal loading up to 62 vol %.	[15]
Two LDPEs + TPE + stearic acid	Stainless steel – 316 L	50 vol%	- successful development of a binder system with two types of soluble polymers for two-step solvent – thermal debinding procedure.	[16]
TPE + grafted polyolefin	CP Ti	55 vol%	- fabrication of high-density pure titanium (≥ 95 density) by optimization debinding and sintering process.	[35]
ABS	Cu and Fe	10–50 wt %	- metal/polymer filaments enable distortion-free 3D metal printing despite thermoplastic expansion.	[13]
PE + paraffin wax + stearic acid	Cu	25, 50, 75 wt%	- employing an innovative method for printing PE by optimization of production parameters at each step.	[20]

* EVA – Ethylene–vinyl acetate, PPC – Poly(propylene carbonate), PLA – Polylactic acid, ATBC – Acetyl tributyl citrate, BVOH – Butenediol vinyl alcohol copolymer, TPE – Thermoplastic elastomer, ABS – Acrylonitrile–butadiene–styrene, LDPE – Low-density polyethylene, PE – Polyethylene.

desirable thermal and mechanical properties after sintering [16]; however, it often compromises the filament's flexibility and printability [25–27]. Binder systems, composed of one or more polymers, are key to managing this trade-off [26,28]. The choice of polymer binder not only governs the dispersion and interfacial compatibility of metal particles within the matrix but also strongly influences the composite's rheological behavior [26,28,29]. This affects both filament flexibility and the material's flow characteristics during extrusion, as well as its thermal stability and mechanical performance throughout the manufacturing process.

In addition to influencing filament flexibility and printability, binder selection plays a crucial role in the subsequent debinding and sintering processes of metal-filled filaments [30–32]. Both complex and simple binder systems have been explored in the literature, each offering specific advantages depending on the material system and targeted properties [30,31,33]. A summary of selected studies is presented in Table 1. For instance, Gloeckle et al. [18] developed a complex binder system consisting of a poly(propylene–ethylene) copolymer with isotactic propylene segments and randomly distributed ethylene units, poly(ethylene–vinyl acetate), poly(isobutene), and stearic acid. Their feedstock demonstrated good FFF printability and suitability for debinding and sintering when the titanium particle loading reached or exceeded 50 vol % [18]. In another study, Wei et al. emphasized the importance of precisely tailoring the binder system. They reported that formulations such as PLA with 10 vol% acetyl tributyl citrate (ATBC), and PLA/butenediol vinyl alcohol copolymer (BVOH) with 5 vol% ATBC, significantly improved the mechanical properties, relative density, and porosity of the final sintered metal parts [34]. Additional examples and formulations from recent studies are summarized in Table 1.

Still in the context of FFF 3D printing, PLA remains one of the most widely used polymers due to its ease of processing, and inherent stiffness [36–40]. However, when used as the sole binder in highly filled metal-polymer systems, PLA's brittleness often leads to filament breakage and reduced printability [15,22,34,41,42]. To enhance flexibility and support continuous extrusion during FFF, recent studies have investigated blending PLA with more ductile polymers [43–45], particularly polyolefins such as polypropylene (PP) or polyethylene (PE) [46–48]. Among these, PE stands out as blending agent for its excellent ductility and toughness, although its low surface energy and limited interlayer adhesion can present challenges for 3D printing.

To address these issues while maintaining a simple and scalable binder formulation, the present study focuses on a binary polymer blend consisting solely of PE and PLA. This strategy aims to leverage the complementary properties of both polymers, combining the mechanical resilience and flexibility of PE with the printability and stiffness of PLA, to optimize the performance of metal-filled filaments in FFF. While PLA is biodegradable, its biodegradability is not necessarily advantageous in this application due to the need for high-temperature processing and material durability. Instead, the sustainability benefit lies in the recyclability of PE. Importantly, the blend also offers a practical pathway for end-of-life separation: PLA can be selectively dissolved from the matrix using appropriate solvents, enabling recovery and recycling of the PE/metal fraction. This facilitates potential reuse of the polymer binder and recovery of metal powders, aligning with circular economy principles in sustainable manufacturing.

In this study, carbonyl nickel (Ni) and water-atomized iron (Fe) were selected as metal fillers for the composite filaments due to their favorable properties and sustainability profiles. Carbonyl Ni, produced via the Mond process [49], is notable for its exceptional recyclability and fine, uniform particle morphology, which enhances dispersion in polymer matrices and improves composite performance. The carbonylation reaction, which occurs below 100 °C at atmospheric pressure and is easily reversible, allows for efficient recovery and reuse of Ni, supporting a closed-loop, environmentally friendly manufacturing cycle. In parallel, Fe powder produced through water atomization offers a clean, low-impact method of fabrication while maintaining high purity and suitable particle characteristics. Together, these powders provide a strong foundation for investigating how metal type, loading, and binder formulation influence the processability and performance of sustainable metal-polymer filaments for FFF 3D printing.

This study focused on the development of metal-filled filaments using PLA/PE binary polymer blends with varying compositions, aiming to enhance filament flexibility without compromising metal loading or printability. The influence of binder composition and metal content on filament morphology, thermal stability, mechanical properties, and 3D printability was systematically investigated. Additionally, the role of metal particle characteristics such as size, shape, and distribution on dispersion and overall composite performance was examined. The fabricated filaments were evaluated for their suitability in debinding and sintering processes, and their performance was benchmarked against commercially available metal-filled filaments. Unlike many existing approaches, our proposed method avoids the use of solvents or additional processing additives, relying instead on a simple,

Table 2
Properties of the polymers (PLA, PE) used as binder.

Polymers	Density (g·cm^{-3})	MFI (g/10 min)
PLA	1.24	8 (210 °C, 2.16 kg)
PE	0.94	25 (190 °C, 2.16 kg)

Table 3
Properties of the metal powders.

Metals	Manufacturing method	Relative density (g·cm^{-3})	Average particles size (μm)
Ni	Mond	8.9	10
Fe	Water-atomized	7.8	120

environmentally friendly binder system. Filaments were produced using a straightforward melt-extrusion process and successfully debinded and sintered in a standard air furnace using only a graphene powder environment to locally reduce the atmosphere. The results provide a basis for designing simpler and more sustainable binder systems for additive manufacturing applications.

2. Material and methods

2.1. Materials

2.1.1. Polymers

In this study, binary polymer blends composed of two immiscible thermodynamically thermoplastic polymers which form a multiphase system were selected as binder systems. The blends were formulated using extrusion-grade, semi-crystalline polylactic acid (PLA, Ingeo Biopolymer 2500HP) supplied by NatureWorks, and a recyclable polyethylene (PE) copolymer functionalized with 12 % maleic anhydride (Fusabond M603) provided by DuPont. Key physical and rheological properties of both polymers are summarized in Table 2. The data was taken from supplier datasheets.

2.1.2. Metal powders

Two types of metal particles were used in this work for metal/polymer filaments fabrication: fine carbonyl nickel powder (100 Series) from VALE and iron powder (ATOMET 1001HP) from Rio Tinto. Most important properties of the metal powders are shown in Table 3. The average particles size presented in the table was taken from supplier datasheets. The data from particle size distribution analysis is presented in the results Section 3.1.

2.2. Metal-filled polymer filaments: manufacturing method

2.2.1. Mixing

Fig. 1 shows a schematic overview that presents the sequence of the different steps in the developed metal-filled polymer filament manufacturing process. PLA/PE binder blends were dried and then physically dry-mixed by hand with either Ni or Fe powders to form the initial feedstock. After dry mixing the polymer-metal composite underwent extrusion to produce filaments suitable for FFF 3D printing. These metal-based filaments were then used to fabricate green parts using a material extrusion-based 3D printer. The printed green parts were subsequently subjected to debinding and sintering in a tabletop furnace to obtain final metal components. All relevant parameters and processing conditions for each step are detailed in the following sections.

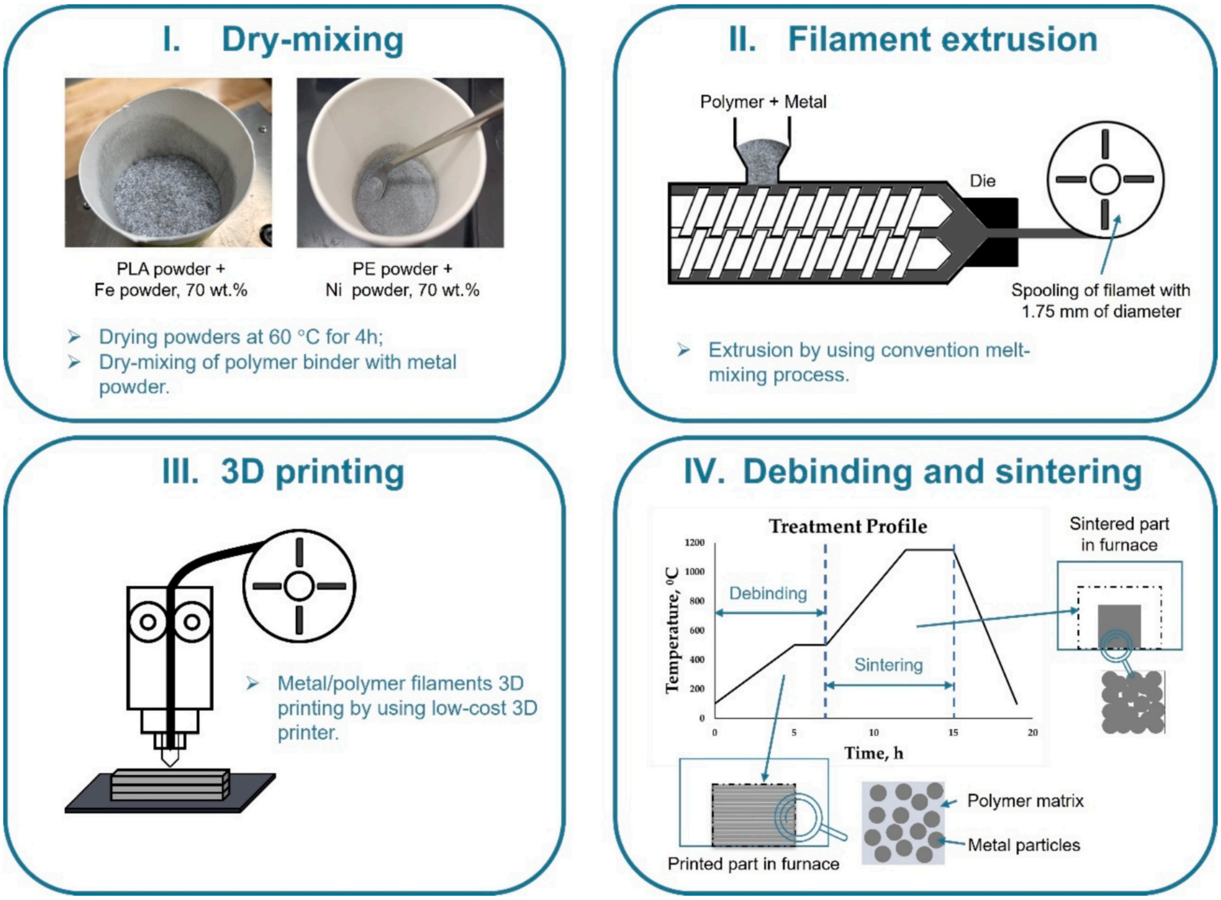

- Drying powders at 60 °C for 4h;
- Dry-mixing of polymer binder with metal powder.

- Extrusion by using convention melt-mixing process.

- Metal/polymer filaments 3D printing by using low-cost 3D printer.

Fig. 1. Schematic overview of the filament manufacturing process steps including the 3D printing process and the produced parts' debinding and sintering.

Table 4

Binder compositions and amount of metal powder in weight used for metal-polymer filament fabrication for the main study.

PE/PLA, wt%	0/100		30/70		70/30		100/0	
Ni, wt%	70	80	70	80	70	80	70	80
Fe, wt%	70	80	70	80	70	80	70	80

Table 5

Conversion of metal powder weight percentage (wt%) to volume percentage (vol%).

Wt% of metal in filament	Vol% of Ni in PE/Ni	Vol% of Ni in PLA/Ni	Vol% of Fe in PE/Fe	Vol% of Fe in PLA/Fe
50	9.6	12.2	10.8	13.7
70	19.8	24.5	21.9	27.1
75	24.1	29.5	26.6	32.3
80	29.7	35.8	32.5	38.9
85	37.4	44.1	40.6	47.4
90	48.7	55.6	52.0	58.9

Note: Conversion based on the density values of the metal powders and polymer binders.

Table 4 shows the compositions of the PLA/PE binder blends used in this study. These binders were physically dry-mixed with carbonyl Ni or water-atomized Fe powders at two weight concentrations (for main study), as listed in Table 3. Prior to mixing, both PLA and PE pellets were shredded into powder form to improve homogeneity. All powders including the metal one were dried at 60 °C for 4 h to eliminate moisture. The polymer-metal mixtures were then compounded using a twin-screw extruder to produce filament. Metal powder contents of 50 wt%, 75 wt%, 85 wt%, and 90 wt% were also investigated to evaluate their effect on filament quality and processability. For clarity and comparison with work reported in literature and commercially available metal-loaded filaments, a conversion table (Table 5) is provided to correlate the studied metal content in weight percent (wt%) with volume percent (vol%). This is important because different studies report metal loading using either wt% or vol%, which can make direct comparisons misleading. Since the physical behavior of highly filled composites such as printability and densification after sintering is more directly influenced by volume fraction, providing a conversion allows for more accurate benchmarking and meaningful comparison with another research in the field.

2.2.2. Extrusion

After dry mixing, the polymer-metal composite, consisting of either a single polymer with metal powder or a polymer blend with metal powder, underwent an extrusion process to produce filaments. Fabrication was performed using a micro twin-screw extruder (HAAKE MiniLab II, Thermo Scientific, USA). The extrusion was carried out at a temperature of 200 °C, with the screws operating at a speed of 30 rpm. The molten filament was extruded through a die with a 2 mm diameter, then drawn and resized to a standard 1.75 mm diameter using a spooler (Felfil Spooler, Italy).

2.2.3. 3D printing

After the extrusion of metal-based filaments, the materials were used to 3D print various specimens using a highly utilized yet low-cost 3D printer, the Creality Ender 3 S1 Pro. Printing parameters and CAD model preparation were managed through Ultimaker® Cura software, which offers precise control over a range of printing variables. To ensure proper adhesion of the printed specimens to the heated bed, a thin layer of adhesive glue was applied prior to printing. Key 3D printing parameters, including nozzle and bed temperatures, printing speed, and other relevant settings, are discussed in detail in the results Section 3.4.

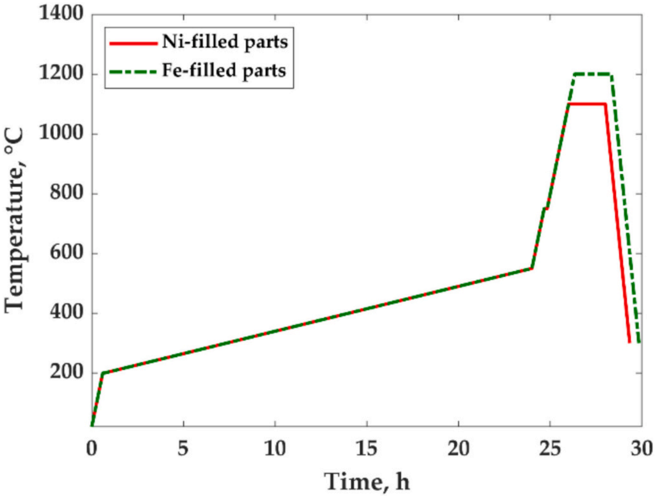

Fig. 2. Debinding and sintering process of the Ni and Fe powder containing 3D printed green parts. (For interpretation of the references to colour in this figure legend, the reader is referred to the web version of this article.)

2.2.4. Debinding and sintering

The 3D-printed green parts were debinded and sintered using a tabletop high-temperature furnace (Pyradia, model F300HP). Fig. 2 illustrates the complete debinding and sintering process for the Ni- and Fe-powder-infused samples used in this study. The process began at 20 °C, with the temperature increased to 200 °C at a heating rate of 5 °C/min. Once 200 °C was reached, the samples were kept for 5 min before starting the debinding process, which continued from 200 °C to 550 °C at a slower heating rate of 0.25 °C/min.

After reaching 550 °C, the sintering process commenced, with the samples heated at 5 °C/min up to 750 °C. At 750 °C, the samples were held for 10 min, then the temperature was increased at a rate of 5 °C/min to the final sintering temperature, 1100 °C for specimens containing Ni powder and 1200 °C for those containing Fe powder. The samples were maintained at their respective final temperatures for 2 h before being cooled to room temperature. Although literature reports successful sintering of Ni and Fe powders at somewhat lower temperatures (typically above ~900 °C), these higher temperatures were selected to ensure sufficient densification within a limited sintering time and to compensate for relatively coarse particle sizes and non-ideal green densities. Furthermore, the samples were kept covered with graphite powder (purified natural flake graphite processed by Nouveau Monde Graphite Inc. with 99.95 % of purity and grain size from 5 μm to 800 μm) throughout the entire debinding and sintering process to prevent oxidation of metal part.

2.3. Characterization

2.3.1. Particles size distribution analysis

The particle size distribution (PSD) of the samples was measured using an LS 13320 XR Particle Size Analyzer (Beckman Coulter, USA) operating in dry mode. Approximately 30 g of metal powder was used for each measurement, both metals were analyzed: iron and nickel. The instrument utilizes laser diffraction to determine particle sizes with high precision. The samples were dried for 2 h at 70 °C before being introduced into the analyzer's dry dispersion unit, ensuring consistent flow and minimizing agglomeration. The refractive index and absorption parameters were set based on the specific properties of iron and nickel. Measurements were conducted at room temperature. The PSD results were reported as volume-based distributions, including the typical cumulative distribution points: median particle size (D50), coarse particle threshold (D90), and fine particle threshold (D10).

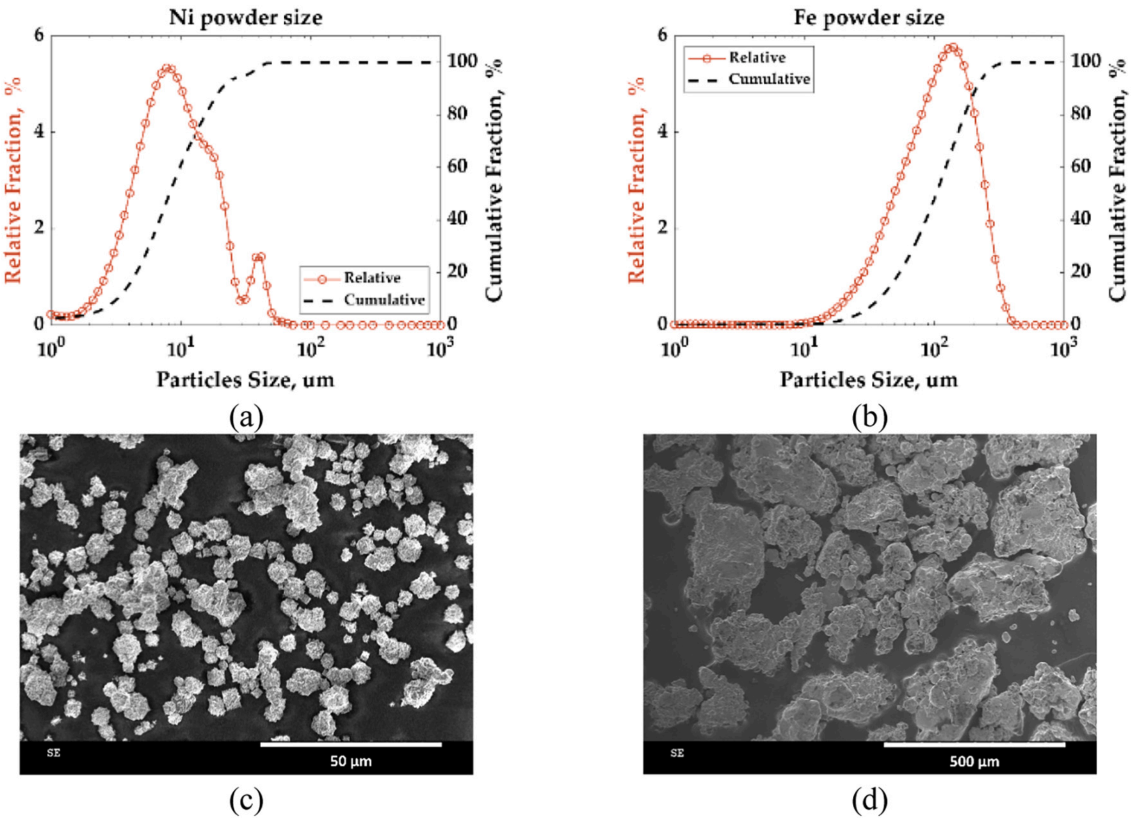

(a) (b)

(c) (d)

Fig. 3. PSD analysis, presented as relative and cumulative fractions, for (a) Ni powder and (b) Fe powder. (c-d) SEM observations for Ni and Fe, respectively. The SEM images are captured at different magnifications to account for the significant difference in average particle size, with Ni particles being approximately ten times smaller than Fe particles.

2.3.2. *Thermal characterization*

2.3.2.1. Thermogravimetric analysis. Thermogravimetric analysis (TGA) was performed for chosen PE/Ni and some PE/PLA/Ni using a PYRIS Diamond TG-DTA instrument. The samples were subjected to a controlled heating program, ranging from 50 °C to 600 °C at a consistent heating rate of 10 °C/min, under a nitrogen atmosphere. This analysis aimed to evaluate the thermal degradation behavior of the binder and accurately determine the actual weight percentage of the metal powder in the filaments.

2.3.2.2. Differential scanning calorimetry: non-isothermal crystallization. All samples were subjected to a thermal treatment starting with heating from 50 °C to 200 °C at a constant rate of 10 °C/min, followed by cooling back to 50 °C at the same rate, under a nitrogen atmosphere. This thermal cycle was repeated twice for each sample to eliminate any prior thermal or mechanical history. Data obtained from the second heating and cooling cycle were used for further analysis. To establish a baseline, the same thermal procedure was first performed using empty pans.

The degree of crystallinity for PE and PLA was determined using the following equation:

$$X_C = \frac{\Delta H}{(1 - \mathrm{w})\Delta H_m} \tag{1}$$

where X_C represents the crystalline weight fraction, ΔH is the measured enthalpy of fusion for the sample, w is the metal powder' weight fraction and ΔH_m is the enthalpy of fusion for 100 % crystalline PE or PLA, with values of 293 J/g and 93 J/g respectively.

2.3.3. *Microscopic characterization*

The cross-sectional morphology of all metal-polymer filaments and green 3D-printed parts was analyzed using scanning electron microscopy (SEM) with a Hitachi TM3000 microscope (Hitachi, Ltd., Tokyo, Japan) in secondary electron mode. Samples were fractured in liquid nitrogen and subsequently coated with gold using a K550X gold sputter coater. Imaging was performed at an accelerating voltage of 15 kV.

2.3.4. *Mechanical characterization*

The tensile properties of the prepared filaments (1.75 mm in diameter) were evaluated using an MTS Alliance RF/200 tensile test apparatus (MTS Systems Corporation, Eden Prairie, MN, USA). Testing was conducted at room temperature, applying a 10 kN load capacity. A crosshead speed of 1 mm/min was used for all metal-powder-filled filaments (Ni or Fe) and neat PLA filaments, whereas a speed of 50 mm/min was applied for unfilled PE filaments and all PE/PLA blend filaments. The primary parameters measured included tensile strength, tensile modulus, and elongation at break. Specimens with a length of 12 cm were extracted from various sections of the filaments to ensure representative sampling and robust statistical analysis. The distance between the specimen grips was set to 8 cm, providing a secure fit within the testing apparatus. Although there is currently no specific ASTM standard for testing thermoplastic filaments, the procedure followed was adapted from ASTM D638 – Standard Test Method for Tensile Properties of Plastics.

2.3.5. *Density measurement*

The density of the sintered Ni blocks was measured at room temperature using a gas pycnometer (Ultrapyc 5000, Anton Paar) with helium as the displacement gas. For each sample, five measurements were taken, and the average density along with the standard deviation is reported in the Results Section 3.5 (Table 9) of this paper.

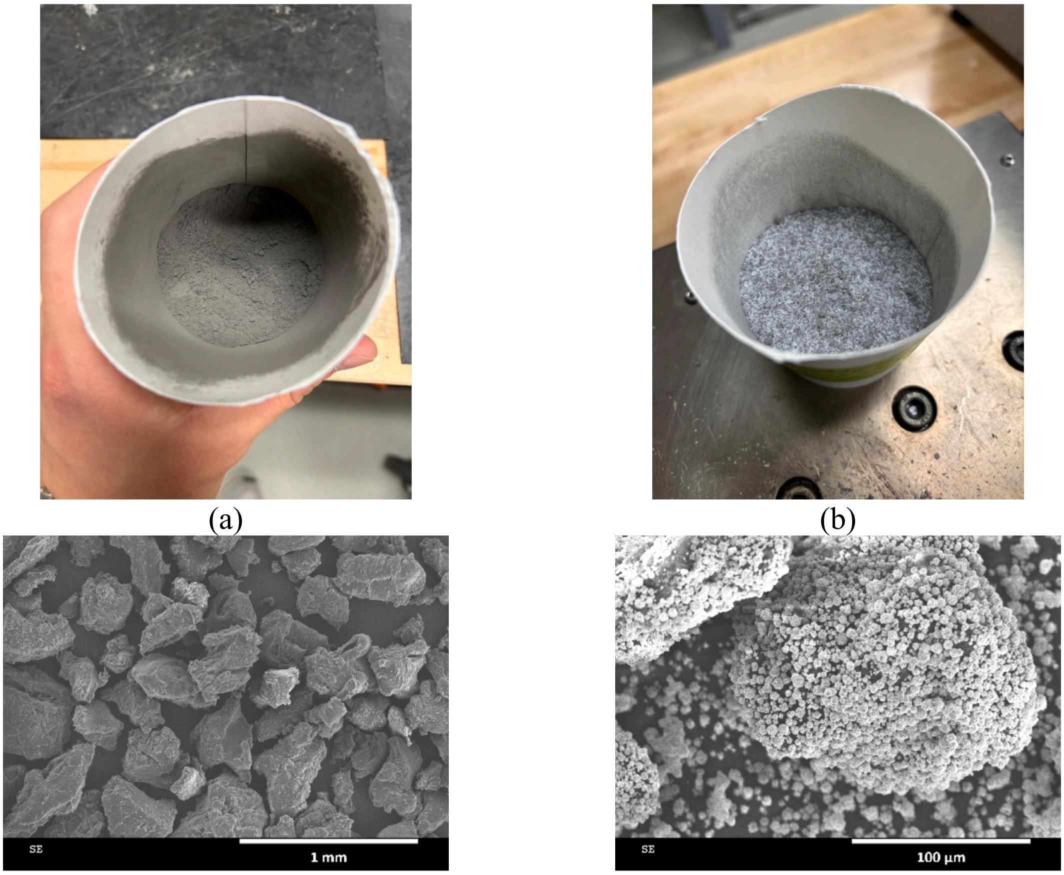

(a) (b) (c) (d)

Fig. 4. (a-b) Photos of dry mix of PE + Ni and PE + Fe with 70 wt% of metal powder, respectively. (c-d) SEM images of neat PE powder (flakes) and PE + Ni powder with 70 wt% of Ni. SEM pictures were taken at different magnifications due to different particles size.

3. Results and discussions

3.1. *Metal-polymer binder: PSD (particle size distribution) and SEM (scanning electron microscopy) analysis of metal powders and dry mix*

PSD and morphology of metal powders significantly affect the processing behavior and properties of metal/polymer composite filaments. To better understand these effects, this analysis aimed to investigate how variations in particle size and geometry influence metal powder distribution within polymer matrices, affect the homogeneity of metal/polymer mixtures, and ultimately impact filament extrusion, 3D printability, and subsequent debinding and sintering behaviors.

Fig. 3 (a) and (b) illustrate the PSD analyses for Ni and Fe powders. The PSD parameters for Ni powder indicate a D10 of 3.4 μm, a median particle size (D50) of 8.6 μm, and a D90 of 21.6 μm. In contrast, the Fe powder exhibits significantly larger particle sizes, approximately an order of magnitude greater than those of Ni, with a D10 of 39.6 μm, a D50 of 108.8 μm, and a D90 of 220.7 μm. These metrics clearly show that the Ni powder has a finer and narrower PSD, whereas Fe powder has a broader and coarser size distribution. Fig. 3 (c) and (d) present SEM images revealing morphological differences between the powders. The Ni particles appear predominantly spherical with a relatively uniform size distribution. Conversely, the Fe particles display significantly irregular shapes characterized by jagged edges, angular features, and a distinctly non-uniform size distribution.

Fig. 4 (a) and (b) present photographs of the chosen dry mixtures of PE + Ni and PE + Fe, each containing 70 wt% metal powder, highlighting the noticeable differences in appearance due to particle size. The smaller Ni particles uniformly cover the polymer flakes, as observed in the SEM image of PE + Ni powder in Fig. 4 (c). This uniform coverage is attributed to the finer size of Ni particles, which allows them to adhere and coat the polymer more effectively. In contrast, the larger Fe particles do not fully cover the polymer flakes, as their size is comparable to that of the polymer particles (see Fig. 4 (d)), resulting in a less homogeneous mixture.

As was mentioned above, the PSD and morphology of metal powders play a crucial role in the extrusion-based production of metal/polymer filaments. Finer particles, such as those in the Ni powder, tend to distribute more uniformly throughout the polymer matrix (see SEM images in Section 3.2), leading to improved packing density and enhanced interfacial interactions between the metal and binder. This homogeneity facilitates smoother extrusion, reduces the risk of nozzle clogging, and improves dimensional accuracy during filament formation. In contrast, it was observed in this work that highly filled Fe-based filaments often exhibit increased swelling during both filament extrusion and 3D printing due to big particles size and non-uniform geometry. Similar effects related to particle size and morphology on flow behavior and printability have been reported in the literature [10,30,50–52].

During the debinding and sintering stages, particles geometry and size also significantly influence the removal of the polymer binder and the densification behavior of the printed parts. Finer particles, due to their higher specific surface area, enhance sintering kinetics through increased diffusion pathways and greater particle contact points. However, these same characteristics may complicate the binder removal process when particles are tightly packed, potentially leading to defects such as cracking or pore entrapment. Moreover, irregular particle shapes, although potentially beneficial for mechanical interlocking, can hinder uniform shrinkage and contribute to anisotropic sintering

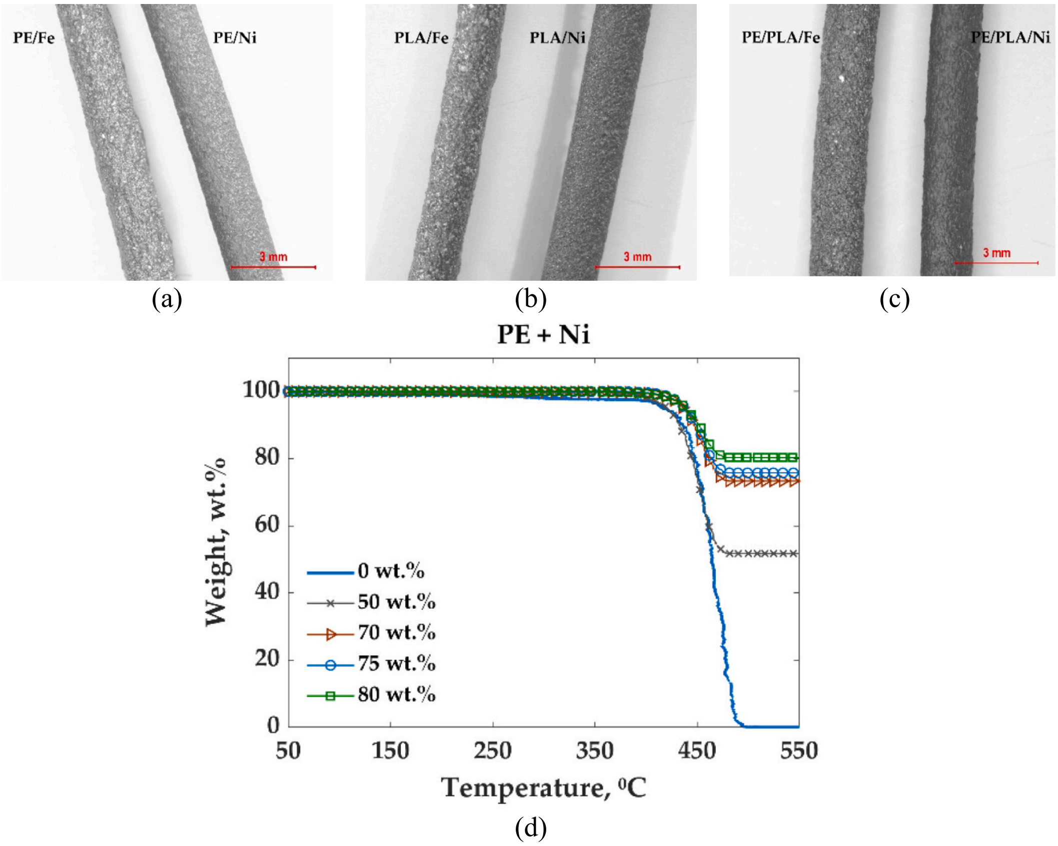

(a) (b) (c)

(d)

Fig. 5. (a) Images of PE/Fe and PE/Ni filaments with 80 wt% of metal loading; (b) PLA/Fe and PLA/Ni filaments with 80 wt% of metal loading (c) PE/PLA/Fe and PE/PLA/Ni blend-based filaments with 80 wt% of metal loading and 70/30 wt% of PE/PLA blend (d) TGA curves for chosen filled PE/Ni filaments and neat PE.

Table 6
Metal weight content prior and after filaments extrusion confirmed with TGA analysis.

PE/Ni filaments	Filament diameter, mm	Metal content, wt%	
		Prior to extrusion	From TGA
50 wt%	1.75	50	51.7
70 wt%	1.75	70	73.4
75 wt%	1.75	75	75.8
80 wt%	1.75	80	80.3

behavior [53,54].

3.2. Metal-polymer filaments: TGA and morphology

In order to assess the impact of metal content and binder composition on filament quality, porosity, flexibility, and thermal stability, composite metal/polymer filaments with various binder systems and metal powder loadings were produced. These properties, critical for printability and performance in FFF, were evaluated through analyses of thermal behavior, morphology, and mechanical integrity. Fig. 5(a–c) present representative images and data for the different composite filaments investigated. Fig. 5 (a) shows PE/Fe and PE/Ni filaments containing 80 wt% metal loads, while Fig. 5 (b) depicts PLA/Fe and PLA/Ni filaments with 80 wt% metal loads. Fig. 5 (c) displays PE/PLA/Fe and PE/PLA/Ni blend-based filaments with 80 wt% metal load and a 70/30 wt% PE/PLA blend. These images demonstrate the high quality of the produced filaments, which exhibit smooth surfaces and consistent structural integrity. The PE-based and PE/PLA blend-based filaments exhibit sufficient flexibility to be easily spooled, in contrast to PLA-based filaments, which become brittle at high metal contents (above 70 wt% for both Ni and Fe powders). This flexibility underscores their suitability for subsequent processing steps, including 3D printing. This flexibility is

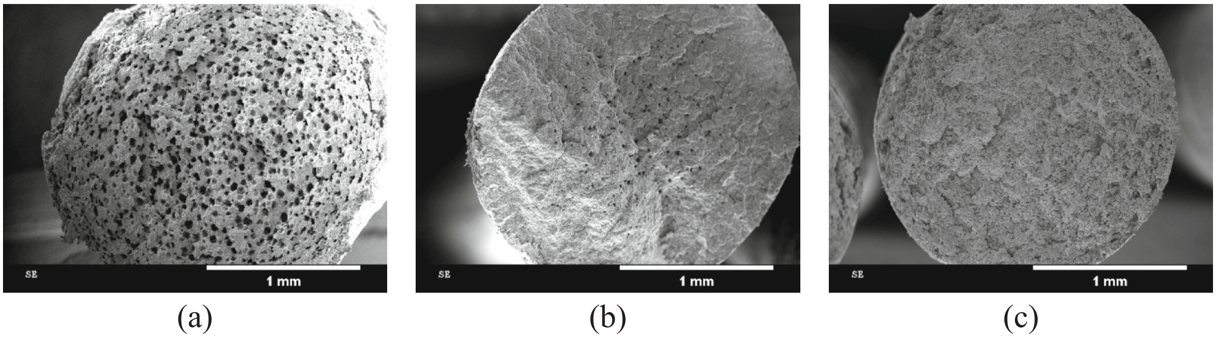

(a) (b) (c)

Fig. 6. SEM images of cross-sections of PE/Ni filaments with: (a) 80 wt%, (b) 85 wt% and (c) 90 wt% of Ni powder.

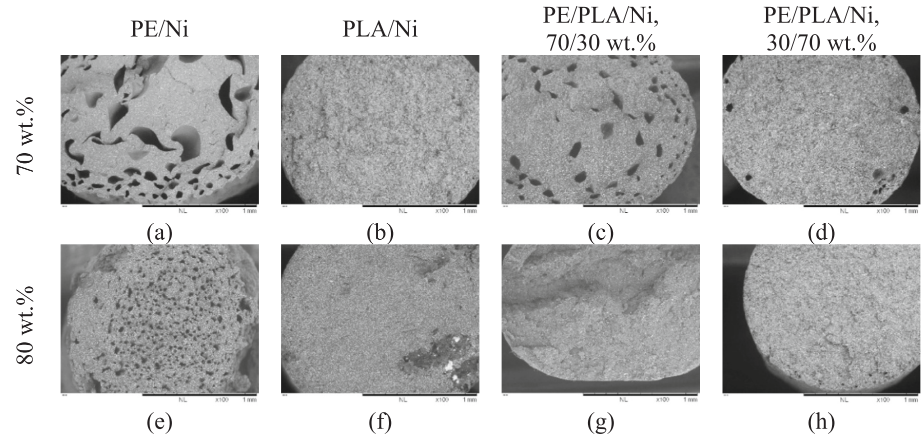

Fig. 7. SEM images of cross-sections of filaments with 70 wt% and 80 wt% of Ni powder for: (a, e) PE/Ni filaments, (b, f) PLA/Ni filaments, (c, g) PE/PLA/Ni filaments with 70/30 wt% of PE/PLA and (d, h) PE/PLA/Ni filaments with 30/70 wt% of PE/PLA.

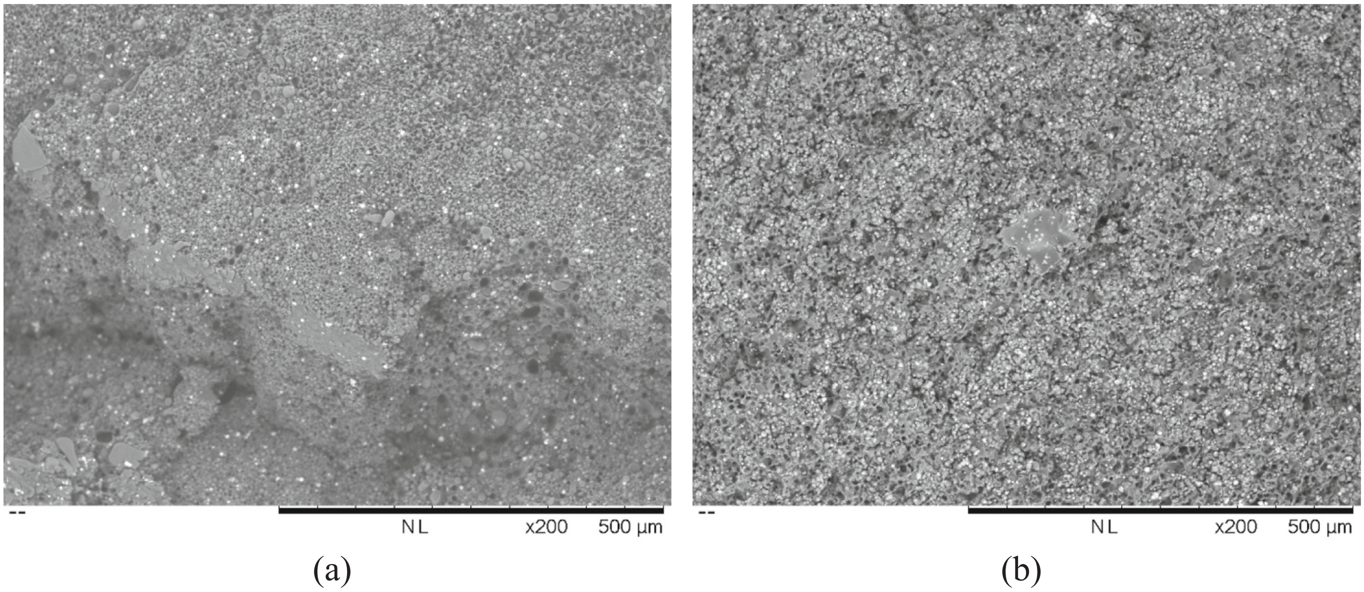

Fig. 8. SEM images of cross-sections of filaments with 80 wt% of Ni powder for different PE/PLA binder composition of: a) 70/30 wt% and b) 30/70 wt%.

particularly advantageous for additive manufacturing applications, where ease of handling and material feed consistency are critical for achieving precise geometries and layer uniformity. Fig. 5 (d) shows typical curves for TGA analysis and Table 6 summarize the results of TGA analysis conducted on chosen PE/Ni composite filaments with varying Ni contents (0–80 wt%). Similar results were obtained for all compositions. TGA measurements reveal that the thermal degradation and combustion of the polymer matrix start above approximately 450 °C. This high degradation temperature indicates that the PE matrix retains thermal stability within the typical processing temperature range of many polymer-based manufacturing techniques, such as extrusion or FDM.

Fig. 6 (a-c) displays SEM cross-sectional images of PE/Ni composite filaments with Ni concentrations of 80 wt%, 85 wt%, and 90 wt%, respectively. These particular compositions were selected to investigate the influence of increasing Ni content on the porosity of the filaments. The SEM images reveal a clear trend: the porosity of the filaments decreases as the Ni content increases. The porosity observed in the PE/Ni filaments results from the combined effect of the high metal loading (up to 90 wt%, porosity reduces with increasing metal content) and the selected processing temperature. An extrusion temperature of 200 °C was chosen as an optimal compromise to ensure adequate flow behavior across all binder–metal compositions. While this temperature provided stable processing for most systems, it was relatively high for neat PE and PE-based composites with lower metal contents (<70 wt%), given the high melt flow index (MFI $\approx$ 20) of PE. Under these conditions, the polymer matrix became excessively fluid, facilitating air entrapment and void formation during extrusion. As the metal content increased beyond 70 wt%, the overall viscosity of the composite also increased, thereby reducing air entrapment and leading to lower porosity. In contrast, PLA/Ni filaments show no porosity even at 70 wt% Ni (see Fig. 7 (b)). However, in this composition, the filaments are brittle, making them unsuitable for practical applications. For this reason, a combination of PE and PLA was selected as the binder material to balance the mechanical properties and porosity control.

Fig. 7 presents SEM images of the cross-sectional morphology of various filament compositions, including PE/Ni and PLA/Ni filaments with 70 wt% and 80 wt% Ni content (Fig. 7 (a-b) and Fig. 7 (e-f), respectively). Additionally, SEM images are shown for filaments containing a binder composed of PE/PLA blends in two different ratios: 70/30 wt% and 30/70 wt% PE/PLA with 70 wt% and 80 wt% Ni (Fig. 7 (c-d) and Fig. 7 (g-h), respectively). Fig. 8 (a-b) presents magnified images of the PE/PLA/Ni filaments with 70/30/80 wt% (Fig. 8 (a)) and 30/70/80 wt% (Fig. 8 (b)) compositions, highlighting the detailed microstructure

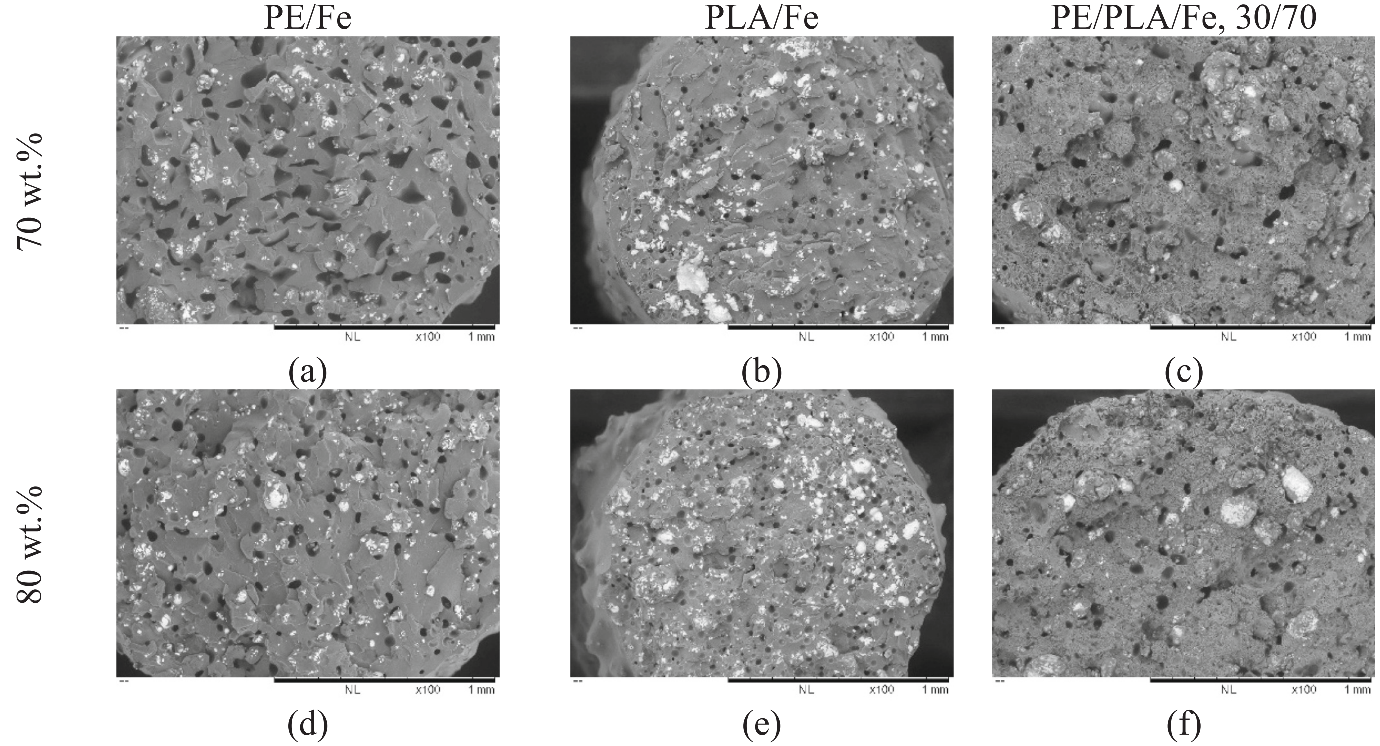

Fig. 9. SEM images of cross-sections of filaments with 70 wt% and 80 wt% of Fe powder for: (a and d) PE/Fe filaments, (b and e) PLA/Fe filaments and (c and f) PE/PLA/Fe filaments with 30/70 wt% of PE/PLA.

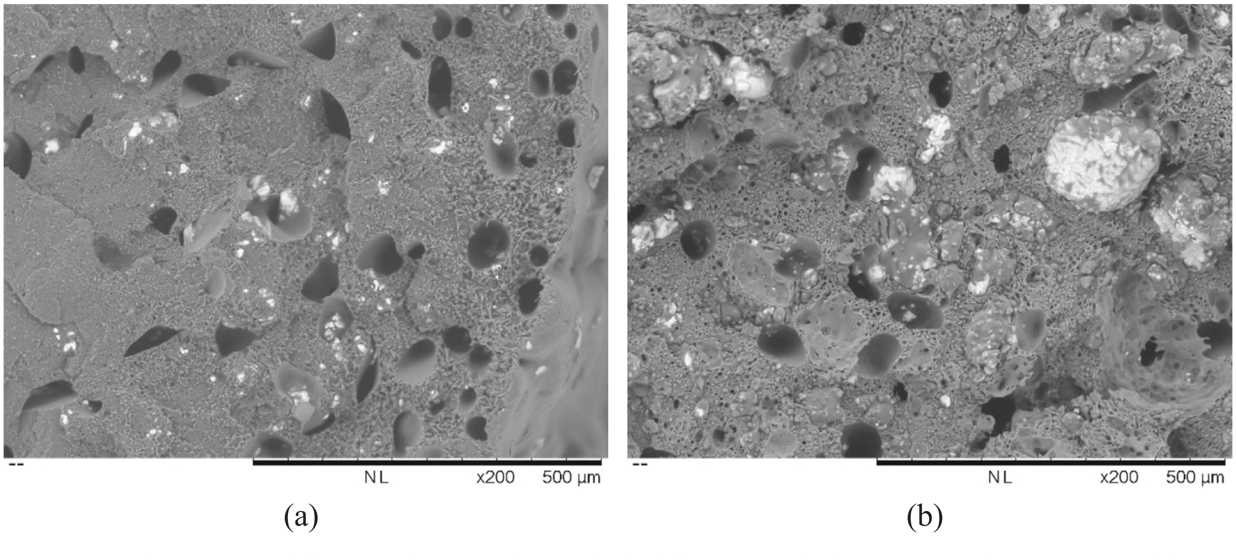

Fig. 10. SEM images of cross-sections of filaments with 80 wt% of Fe powder for different PE/PLA binder composition of: a) 70/30 wt% and b) 30/70 wt%.

and particle distribution. As was mentioned above, the SEM images reveal a notable reduction in filament porosity with increasing Ni content. Filaments containing 80 wt% Ni exhibit significantly lower porosity compared to those with 70 wt% Ni, regardless of the binder composition. This trend aligns with expectations, as higher Ni loading increases the volume fraction of metallic particles, thereby minimizing the void space within the polymer-metal matrix. The binder composition also plays a critical role in determining filament porosity. Filaments incorporating PE/PLA blends as the binder exhibit a more complex microstructure, with porosity influenced by both the Ni content and the ratio of PE to PLA. Filaments with a higher proportion of PE (70/30 wt% PE/PLA) tend to exhibit slightly higher porosity compared to those with a higher PLA content (30/70 wt% PE/PLA), even at the same Ni loading. This difference arises from the intrinsic properties of the two polymers. PE, being softer and possessing lower surface energy, enhances ductility but provides weaker particle–matrix adhesion due to reduced wetting, which in turn increases the likelihood of void formation during processing. In contrast, PLA, with its higher viscosity and stiffness, mitigates void formation by promoting better particle packing. However, PLA’s brittle nature can lead to less uniform dispersion and bonding of Ni particles within the matrix, introducing challenges in maintaining homogeneity. These distinct polymer behaviors underscore the importance of binder selection in achieving optimal filament porosity and mechanical properties.

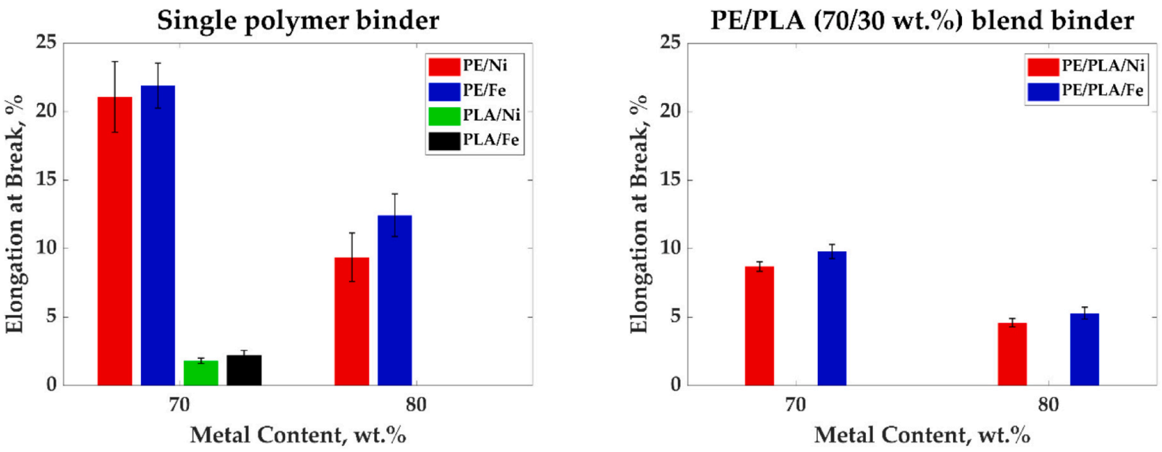

(a) (b)

Fig. 11. Elongation at break as a function of metal content for: (a) metal filaments with single polymer as a binder and (b) metal filaments with PE/PLA (70/30 wt%) polymer blend as a binder.

Fig. 9 presents SEM images of the cross-sectional morphology of filaments containing different binders and filled with Fe particles. The samples include PE/Fe and PLA/Fe filaments with Fe contents of 70 wt% and 80 wt% (Fig. 9 (a-b) and 9 (d-e), respectively), as well as PE/PLA/Fe filaments with a 30/70 wt% PE/PLA binder and Fe contents of 70 wt% and 80 wt% (Fig. 9 (c and f)). Fig. 10 (a-b) presents magnified images of the PE/PLA/Fe filaments with 70/30/80 wt% (Fig. 10 (a)) and 30/70/80 wt% (Fig. 10 (b)) compositions, highlighting the detailed microstructure and particle distribution. Unlike the trends observed in Ni-filled filaments, the porosity in these Fe-filled filaments is not significantly influenced by either the Fe content or the binder composition. Specifically, increasing Fe content does not result in a substantial reduction in porosity, regardless of whether the binder is composed of PE, PLA, or a PE/PLA blend. This suggests a weaker correlation between particle loading and porosity for Fe-based filaments compared to Ni-based filaments, potentially due to differences in particle morphology, packing behavior, or interaction with the binder matrix.

3.3. *Metal-polymer filaments: mechanical properties*

In order to understand how binder composition and metal content influence filament flexibility and suitability for 3D printing the evaluation of the mechanical behavior of metal/polymer filaments, specifically, the tensile tests were done. Both single-polymer matrices (PE or PLA) and PE/PLA blends with varying ratios were studied in combination with high metal loading (Ni and Fe powders).

Fig. 11 (a–b) illustrate the elongation at break as a function of metal content (Ni and Fe) for filaments with varying binder compositions. These binders include single-polymer matrices (either PE or PLA; Fig. 11 (a)) and PE/PLA polymer blends in ratios of 70/30 wt% and 30/70 wt% (Fig. 11 (b)). The data show that PE-based filaments exhibit significantly higher elongation at break than PLA-based filaments. This is expected, as neat PE filaments demonstrate an inherently high elongation at break (140 % ± 15 %), while neat PLA filaments display a much lower value (7.6 % ± 0.9 %).

However, incorporating high metal powder content (~80 wt%, Ni or Fe) substantially reduces the elongation at break in both PE- and PLA-based filaments. This reduction is particularly severe in PLA/Ni filaments with 80 wt% Ni, where specimens were too brittle to be tested. Although PE-based filaments offer greater flexibility, they present challenges for 3D printing, as discussed in the introduction.

For filaments employing a PE/PLA blend binder with a 70/30 wt% ratio, the elongation at break is comparable to that of commercially available metal-filled filaments, such as BASF filaments containing stainless steel particles or Virtual Foundry filaments with copper particles (see Table 7 for comparison). In contrast, filaments with a 30/70 wt% PE/PLA ratio demonstrate higher elongation at break than PLA-only filaments; however, their elongation is approximately half that of filaments with the 70/30 PE/PLA blend. Despite this reduction, these filaments remain suitable for 3D printing and are capable of producing high-quality green parts (see Section 3.4).

Table 7
Elongation at break properties comparison for metal filaments obtained in this work compared to industrially available metal filaments.

Filaments	Binder content, wt%	Metal content, wt %	Elongation at break, %	UTS, MPa	E, GPa
316 L SS BASF*	Complex, ([56])	90	5.4 ± 0.9	10.2 ± 0.1	1 ± 0.09
PLA/Cu VF*	Complex	90	8.7 ± 1.4	17 ± 0.3	1.7 ± 0.1
PE/PLA/Ni	70/30	70	8.7 ± 0.4	11.5 ± 0.3	0.7 ± 0.03
PE/PLA/Fe	70/30	70	9.8 ± 0.5	10.1 ± 0.1	0.5 ± 0.02
PE/PLA/Ni	70/30	80	4.6 ± 0.3	8.1 ± 0.3	0.8 ± 0.01
PE/PLA/Fe	70/30	80	5.3 ± 0.4	8 ± 0.7	0.5 ± 0.01
PE/PLA/Ni	30/70	70	3.4 ± 0.1	15.5 ± 0.2	1.2 ± 0.1
PE/PLA/Fe	30/70	70	4.5 ± 0.3	21.4 ± 2.9	1.1 ± 0.1
PE/PLA/Ni	30/70	80	2.5 ± 0.2	12.5 ± 1	1.3 ± 0.1
PE/PLA/Fe	30/70	80	4 ± 0.5	11.2 ± 2.4	1 ± 0.09

[*] 316 L stainless steel filaments (with complex binder system) from BASF and PLA/Cu filaments from Virtual Foundry.

In addition to elongation at break, the ultimate tensile strength (UTS) and elastic modulus (E) were also determined to provide a more complete assessment of the mechanical performance of the metal-filled filaments. As summarized in Table 7, UTS values range between 8 and 21 MPa depending on metal type, metal loading, and binder ratio, while the modulus varies from 0.5 to 1.3 GPa. These results reveal that filaments with a higher PLA content (30/70 PE/PLA) generally exhibit greater stiffness (higher E) and strength (higher UTS), consistent with the inherently rigid nature of PLA. Conversely, filaments with a 70/30 PE/PLA ratio show lower modulus and strength but superior flexibility. Increasing the metal content to 80 wt% reduces both UTS and

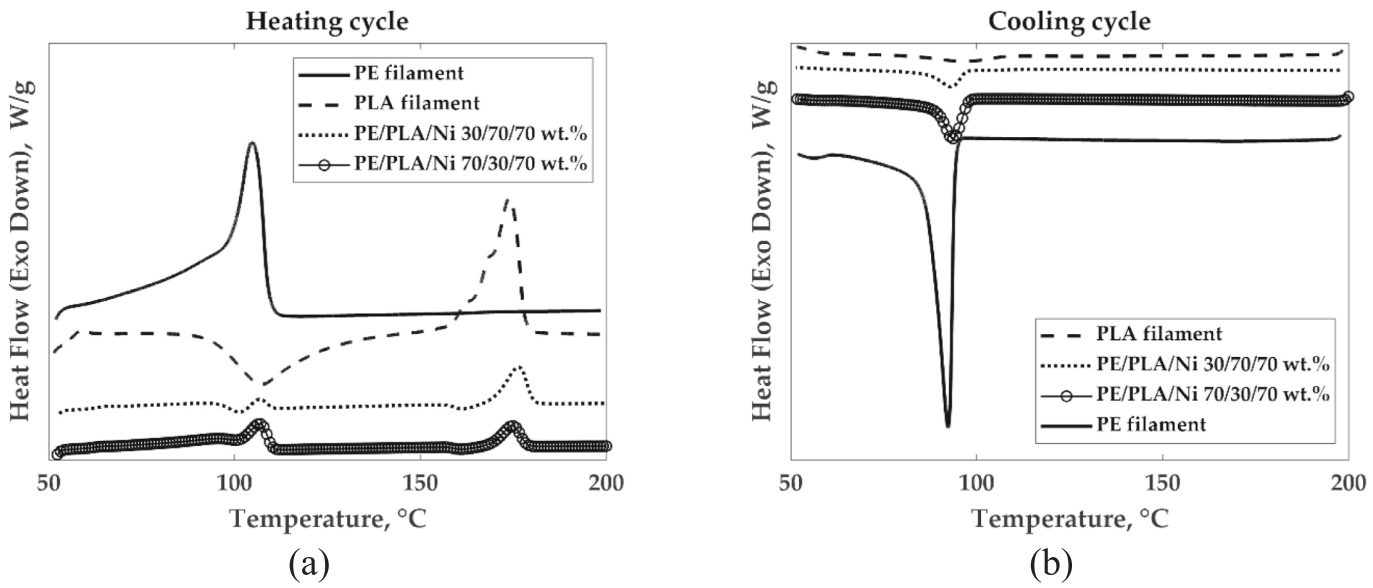

Fig. 12. Effect of PE/PLA blend composition and metal content on non-isothermal crystallization of different filaments during heating (a) and coiling (b).

elongation, which is expected due to reduced polymer continuity and load transfer efficiency within the filament microstructure.

In conclusion, blending PE with PLA improves the flexibility of the filaments compared to PLA-only binders while preserving acceptable printability, as discussed in the following section. Moreover, the measured UTS and modulus values confirm that the mechanical properties of the developed filaments are within the same order of magnitude as those of industrially available metal/polymer filaments, further supporting their potential for AM applications. It is worth noting that the reported mechanical property values are of the same order of magnitude as those observed in other studies on metal/polymer filaments, which also demonstrated good printability of such materials [8,9,11,55].

3.4. *Metal-polymer filaments: 3D printing*

Several critical printing parameters significantly influence the quality of components fabricated via FFF using metal/polymer composite filaments, particularly printing temperature, bed temperature, printing speed, and layer height [12,57–59]. The careful optimization of these parameters is essential for producing dimensionally accurate, mechanically robust, and defect-free printed parts, which consequently facilitates effective debinding and sintering processes and ensures the attainment of fully dense metallic components. Notably, the metal/polymer composite filaments developed in this study exhibit a distinct advantage: they require only minimal parameter adjustments due to their relatively narrow processing windows, consistently yielding high-quality prints. This ease of printability contrasts favorably with many commercially available metal/polymer filaments, which typically necessitate extensive parameter tuning to achieve acceptable results.

In order to gain a deeper understanding of the thermal behavior of filaments during 3D printing and to optimize the printing process for the developed composite filaments, DSC analysis was performed. This analysis identifies key thermal transitions, including melting points, crystallization temperatures, and the degree of crystallinity of the binder components, PE and PLA. The DSC results support the rational selection of extrusion and bed temperatures for each formulation. This thermal characterization is particularly important for composite filaments composed of mixed polymer matrices, where interactions between components may shift thermal transitions and affect overall processability.

Fig. 12 illustrates the crystallization behavior of neat PE and PLA filaments, as well as PE/PLA/Ni composites with varying binder compositions. Specifically, Fig. 12 (a) presents the heating cycle results for all filaments, while Fig. 12 (b) shows the corresponding cooling cycle data. During the heating cycle, the melting peak of the PE filament appears at a significantly lower temperature (105 °C) compared to that of PLA (174 °C). The PE/PLA-based filaments containing 70 wt% Ni exhibit melting transitions corresponding to both PE and PLA components. Notably, the melting temperatures are slightly elevated relative to the neat polymers, which is attributed to the presence of a high metal content (Ni), whose superior thermal conductivity alters the thermal response of the polymer matrix.

Table 8
Melting and crystallization temperatures, enthalpy and degree of crystallinity of neat PE and PLA filaments, and PE/PLA/Ni filaments with 30/70/70 wt% and 70/30/70 wt% filament compositions.*

Filaments	T_{m1}, °C	T_{m2}, °C	T_c, °C	T_{cc}, °C	$\Delta H_{1/2}, J/g$	X_{C1}, %	X_{C2}, %
PE	105	–	92.3	–	73.4	25	23.2
PLA	–	174	–	107.6	47	50	–
PE/PLA/Ni, 30/70/70 wt%	106.5	176	93	101.3	10.7 + 1.9 (PLA + PE)	40.5	9.8
PE/PLA/Ni, 70/30/70 wt%	107.1	174.5	93.4	–	5.3 + 3.7 (PLA + PE)	23.2	17.2

[*] T_{m1} is the melting temperature for PE; T_{m2} is the melting temperature for PLA; T_c is the crystallization temperature; T_{cc} is the cold crystallization temperature; $\Delta H_{1/2}$ is the measured enthalpy of fusion for PE or PLA; X_{C1} is the degree of crystallinity calculated from melting curve; X_{C2} is the degree of crystallinity calculated from crystallization curve.

Neat PLA also exhibits a cold crystallization phenomenon, which is partially retained in the composites; however, it is largely masked by the prominent melting peak of PE. During the cooling cycle, PLA shows no crystallization peak, whereas both neat PE and the PE/PLA/Ni composites exhibit distinct crystallization peaks. The degree of crystallinity was calculated using Eq. (1) (refer to Methodology Section 2.3.2.2) from both the heating (X_{C1}) and cooling (X_{C2}) curves for all compositions. The crystallinity values for the Ni-filled filaments are influenced by the contributions from both PE and PLA. These polymers crystallize differently upon cooling, and the presence of PLA, which lacks a distinct crystallization peak, leads to a reduction in the overall crystallization

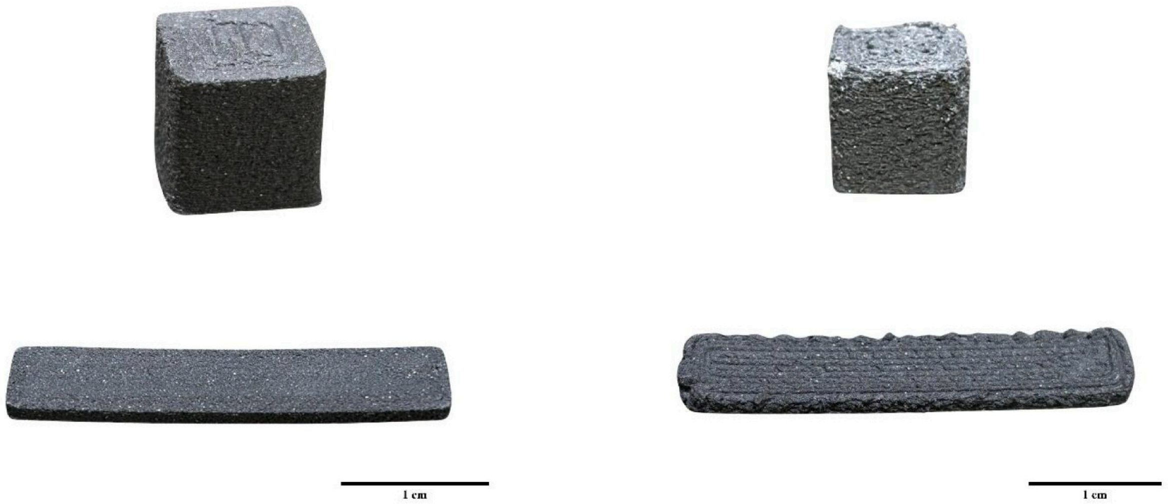

- Printing temperature: 240 °C
- Bed temperature: 100 °C
- No cooling
- Printing speed: 15 mm/s
- Layer height: 0.2 mm

(a)

- Printing temperature: 220 °C
- Bed temperature: 60 °C
- No cooling
- Printing speed: 25 mm/s
- Layer height: 0.2 mm

(b)

Fig. 13. Influence of printing parameters on print quality for Fe-based composite filaments (PE/PLA/Fe 30/70/80 wt%).

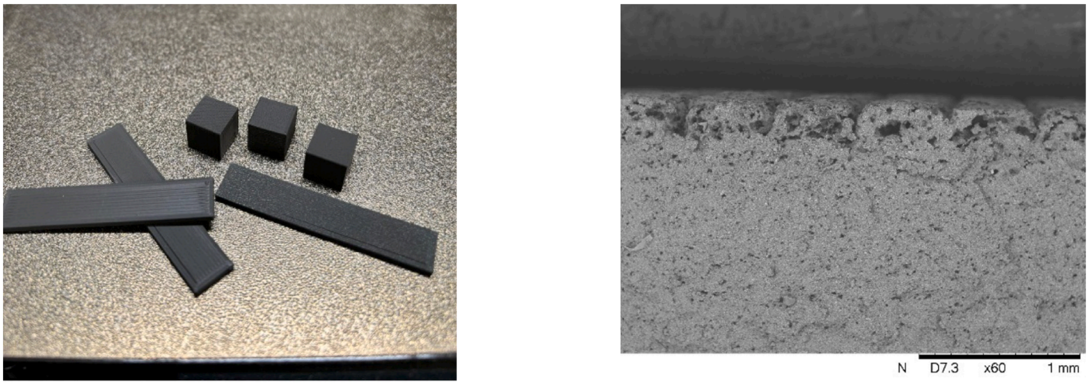

(a) (b)

Fig. 14. (a) Optimized 3D-printed parts of Ni-based composite filaments; (b) Printing surface quality for green parts of Ni-based composite filaments. (For interpretation of the references to colour in this figure legend, the reader is referred to the web version of this article.)

peak intensity in the Ni-filled composites compared to pure PE. All measured thermal properties, including melting temperatures, crystallization temperatures, and degrees of crystallinity, are summarized in Table 8.

Fig. 13 (a–b) illustrates representative photographs comparing the print quality of PE/PLA/Fe 30/70/80 wt% composite filaments, fabricated under varying printing conditions. As clearly depicted, the extrusion temperature, bed temperature, and printing speed significantly impact the visual and dimensional quality of the final parts. Optimized parameters identified for Fe-based composite filaments across all tested compositions include an extrusion temperature of 240 °C, bed temperature of 100 °C, printing speed of 15 mm/s, and a layer height of 0.2 mm (Fig. 13 (a)). A nozzle diameter of 1.0 mm was selected to accommodate the relatively larger Fe particles employed, as previously established. Conversely, Ni-based composite filaments (for all compositions) exhibited optimal print quality under slightly reduced temperatures, specifically an extrusion temperature of 220 °C, bed temperature of 60 °C, printing speed of 20 mm/s, and the same layer height of 0.2 mm. Additionally, a smaller nozzle diameter of 0.4 mm was employed, aligned with the finer PSD of the Ni powder. Fig. 14 (a) shows a photograph of optimized printed samples of the PE/PLA/Ni (30/70/80 wt%) composite, while Fig. 14 (b) presents an SEM image of a cross-section from one of the 3D-printed samples, illustrating the representative surface quality of the Ni-filled composites. It should be noted, that both PE/PLA binder ratios (70/30 and 30/70 wt%) were successfully used for 3D printing and subsequent sintering of metallic structures. The overall printing quality, dimensional accuracy, and sintered part integrity were comparable for both systems. For clarity, Figs. 13 and 14 present the PE/PLA (30/70 wt%) composition as a representative example of the optimized printed and sintered samples, as the results obtained for the 70/30 composition showed similar characteristics and microstructural features.

(a) Neat PE

(b) PE/PLA, 50/50 wt.%

(c) PE/Ni, 70wt.% of Ni

(d) PE/Fe, 70wt.% of Fe

Fig. 15. Comparison of printed components fabricated from (a) neat PE, (b) PE/PLA (50/50 wt%) blend, and PE-based metal composites containing 70 wt% metal powder: (c) PE/Ni, (d) PE/Fe.

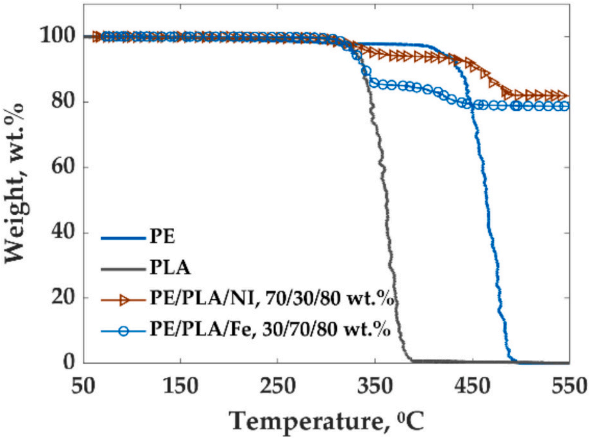

Fig. 16. GA of extruded PE, PLA, and PE/PLA/Ni and PE/PLA/Fe filaments, indicating distinct degradation steps for each polymer phase and residual Ni content.

Experimental observations also highlighted significant challenges in the direct 3D printing of metal-filled filaments based on only PE (i.e., PE/Ni and PE/Fe). Although PE-based filaments (containing any amount of metal powder) showed improved flexibility compared to PLA-based filaments, their inherently lower stiffness and greater ductility introduced considerable difficulties, such as unstable extrusion and inconsistent print quality. Frequent nozzle clogging, compromised dimensional precision, and poor interlayer adhesion characterized attempts at printing neat PE-based composite filaments. Consequently, incorporating PLA into the polymeric binder was essential to achieving a more balanced formulation that markedly enhanced filament processability while retaining acceptable mechanical properties, as discussed earlier. Fig. 15 demonstrates two printed samples for each example comparing neat PE (a), a PE/PLA (50/50 wt%) blend (b), and PE-based composites containing 70 wt% metal powder: PE/Ni (c) and PE/Fe (d).

It should be noted that the Ni and Fe powders employed in this study differ substantially in morphology and particle size, with Ni exhibiting a fine spherical shape and Fe presenting a coarser, irregular morphology as was already discussed above. These inherent differences inevitably influence flowability, packing, and sintering behavior. Therefore, the intention of this work was not to perform a direct comparison between Ni- and Fe-based systems, but rather to demonstrate the applicability of the developed PE/PLA-based binder systems across different types of metallic powders. The similar processing behavior and printability achieved in both cases highlight the robustness and versatility of the binder formulation rather than the specific performance of one metal over the other.

3.5. Debinding and sintering

Following the extrusion and 3D printing of metal-filled filaments, the printed green parts must undergo debinding and sintering to remove the polymeric binder and achieve a fully metallic, dense structure. This step is crucial for transforming the shaped part into a functional metal component with desirable mechanical and structural properties. The debinding process eliminates the polymer matrix without damaging the geometry of the part, while sintering promotes particle bonding and densification through diffusion at elevated temperatures. However, these processes must be carefully optimized to prevent issues such as oxidation, cracking, and excessive porosity.

Fig. 16 presents the TGA results for extruded PE, PLA, and Ni-filled and Fe-filled PE/PLA filaments. Thermal degradation of the polymer components was clearly observed: PE began to degrade at approximately 350 °C, while PLA degradation initiated around 250 °C. As a result, both PE/PLA/Ni (70/30/80 wt%) and PE/PLA/Fe (30/70/80 wt%) composite filaments exhibited a two-step degradation profile, where the first stage corresponds to the decomposition of the PLA phase, and the second to the degradation of the PE phase. The residual mass at the end of the TGA run corresponds to the non-volatile metallic content (i.e., nickel or iron), confirming the successful loading of metal powder into the filament. Based on the onset of degradation at ~250 °C, the thermal debinding process was initiated at 200 °C, applying a very low heating rate to avoid internal pressure buildup or part deformation due to rapid gas evolution.

Fig. 17 (a) shows a typical additively manufactured green part (metal/polymer composite cube) fabricated using a filament loaded with 80 wt% metal powder. During sintering, oxidation is a significant concern, particularly for reactive metals like nickel. Fig. 17 (b) and 17 (c) compare sintered Ni structures without and with graphite powder coverage, respectively. When no protective graphite was used (Fig. 17 (b)), the sintered structure developed a greenish hue, indicative of surface oxidation. This oxidation not only alters appearance but also severely impairs densification, as observed in the foamy and porous

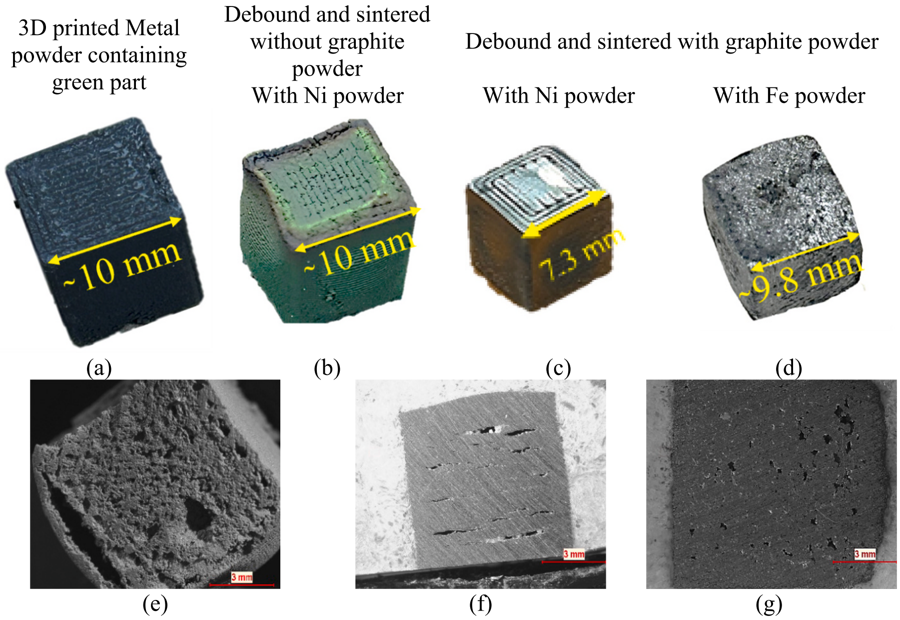

Fig. 17. (a) 3D-printed green parts, (b) sintered Ni structure without graphite powder covering the sample, (c) sintered Ni structure, and (d) sintered Fe structure with graphite powder used to cover the samples. Additionally, (e) optical microscope (OM) image of the sintered Ni microstructure without graphite powder covering the sample, and OM images sintered (f) Ni microstructure and (g) Fe microstructure with graphite powder used to cover the samples during sintering. (For interpretation of the references to colour in this figure legend, the reader is referred to the web version of this article.)

Table 9
Density values for sintered Ni cubes fabricated from 3D-printed green parts with 80 wt% Ni content.

Sample	Observed density of the sintered part		Fully dense Ni, g/cm3
	g/cm3	%	
1	8.512 ± 0.014	95.6	
2	8.507 ± 0.016	95.6	8.9
3	8.376 ± 0.027	94.1	

microstructure in Fig. 17 (e).

In contrast, using graphite powder as a protective barrier during sintering effectively created a reducing atmosphere, preventing oxidation. Consequently, sintered Ni and Fe structures displayed dense, metallic microstructures, as shown in Fig. 17 (f) and 17 (g). These samples retained their metallic luster and exhibited significantly reduced porosity, supporting the importance of inert or reducing sintering conditions. Although the Ni and Fe structures demonstrated good densification, small residual porosity remained in both. This could be further minimized by optimizing debinding and sintering parameters, such as heating rate, holding time, peak temperature, and atmosphere, as reported in related literature [12,30,35,56,60].

Moreover, differential shrinkage behavior was observed. The Ni cubes experienced more pronounced shrinkage than the Fe cubes, likely due to the higher thermal expansion coefficient of Ni, which contributes to more substantial contraction during cooling. While dense structures were achieved for both metals, larger and more visible cracks were present in some Ni samples. This could be attributed to several factors:

- Particle size distribution: the Ni powder used was approximately 10 times finer than the Fe powder. Finer powders tend to pack more densely but are also more susceptible to cracking due to lower green strength and increased capillary forces during binder burnout.
- Loosening effect: The “loosening effect” refers to particle rearrangement and void formation during binder removal, which may be more pronounced in fine Ni powders, leading to poor neck formation during sintering.
- Higher shrinkage stress: due to greater shrinkage, internal stresses during cooling are amplified in Ni parts, which could exceed the fracture toughness of the sintered structure, promoting crack formation.

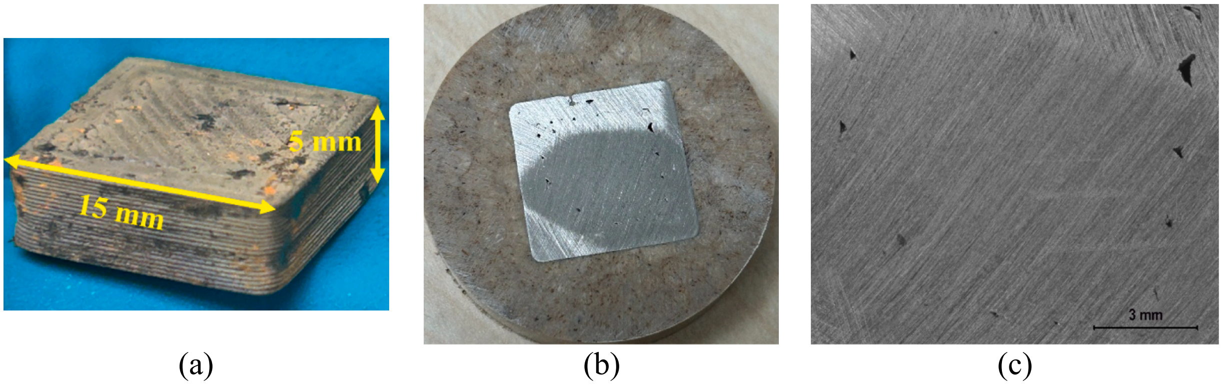

Fig. 18. (a) Sintered Ni block (15 × 15 × 5 mm); (b–c) Cross-sectional microstructure images showing high density and particle fusion.

Table 9 presents the measured densities of sintered Ni blocks produced from green parts containing 80 wt% Ni powder. The pycnometric method was selected for its high accuracy in determining true (skeletal) density. Minor open porosity was observed on the surface of some sintered samples, which is consistent with the high metal loading and the absence of full densification after sintering. These pores, however, were isolated and did not significantly influence the bulk density values obtained. The results demonstrate that densities close to the theoretical density of pure Ni can be achieved through the FFF and post-processing route employed in this study.

To illustrate the dimensional changes and microstructure quality, Fig. 18 (a) shows a sintered Ni cube (15 × 15 × 5 mm) originally printed as a 20 × 20 × 7 mm green part, highlighting a linear shrinkage of approximately 25 %. Cross-sectional micrographs in Fig. 18 (b) and (c) further validate the densification, with the internal structure showing minimal porosity and good particle bonding. These microstructures were revealed after simple surface sanding, confirming bulk densification and surface integrity suitable for post-machining or surface treatments.

4. Conclusion

Highly loaded metal/polymer filaments based on PE, PLA, and PE/PLA blends with up to 90 wt% Ni and 80 wt% Fe were successfully developed via twin-screw extrusion and used for fused filament fabrication of metallic components. PSD analysis showed that Ni powder (D50 = 8.6 μm) with spherical morphology resulted in significantly more homogeneous polymer-metal mixtures compared to Fe powder (D50 = 108.8 μm), which had irregular, angular particles. The use of PE/PLA binder systems allowed for tunable mechanical properties, where a 70/30 wt% PE/PLA blend containing 80 wt% Ni achieved an elongation at break of 18.6 %, compared to <1 % for PLA-only composites and offered an optimal balance between flexibility and strength. Filaments with 80–90 wt% Ni exhibited the lowest porosity, while PLA-rich blends (30/70 PE/PLA) improved interfacial particle bonding. 3D printing was optimized at 220 °C/60 °C for Ni-filled filaments (0.4 mm nozzle) and 240 °C/100 °C for Fe-filled filaments (1.0 mm nozzle). Thermal analysis revealed two distinct degradation steps in the PE/PLA/Ni filaments at ~250 °C and ~ 350 °C, corresponding to PLA and PE decomposition, respectively. TGA results established the degradation profiles of PE and PLA, informing the thermal debinding protocol. Successful debinding was achieved beginning at 200 °C with slow ramp rates, and sintering in graphite-covered conditions (in order to reach reduced atmosphere conditions) produced dense metallic structures. Ni-based sintered samples showed ~25 % shrinkage and densities reaching 7.9 g/cm^3 (98 % of theoretical) but exhibited microcracks due to fine powder size and thermal mismatch. In contrast, Fe-based samples exhibited fewer defects and lower shrinkage. By utilizing a straightforward dry-mixing method with simple polymer blends, this approach eliminates the need for complex multi-step processing or hazardous solvents, offering a more sustainable and scalable route for producing highly filled metal/polymer filaments suitable for FFF-based fabrication of metallic parts. By optimizing binder composition, powder selection, and sintering conditions, high-density, structurally sound metal components can be additively manufactured.

Future work may focus on refining the debinding and sintering profiles to further reduce porosity and enhance mechanical performance, as well as exploring other metal systems and binder combinations to extend the approach to a broader range of materials and applications. Additionally, the use of carbonyl Fe powders having particle sizes comparable to carbonyl Ni and mixtures of carbonyl Fe + Ni could provide a promising pathway toward the fabrication of Fe—Ni alloys such as Invar (approximately 70 % Fe, 30 % Ni), known for their exceptional dimensional stability. The potential availability of custom-produced ultrafine sub-micron carbonyl powders may further enable high-performance alloy development through this additive manufacturing approach.

CRediT authorship contribution statement

Daria Strugova: Writing – review & editing, Writing – original draft, Visualization, Validation, Software, Methodology, Investigation, Formal analysis, Data curation, Conceptualization. **S.M. Nourin Sultana:** Writing – review & editing, Methodology, Investigation, Formal analysis, Data curation. **Jean-Philippe Leclair:** Writing – review & editing, Methodology, Investigation, Data curation. **Éric David:** Writing – review & editing, Validation, Supervision, Methodology, Conceptualization. **Nicole R. Demarquette:** Writing – review & editing, Validation, Supervision, Resources, Methodology, Funding acquisition, Conceptualization. **Vladimir Paserin:** Writing – review & editing, Validation, Resources, Methodology, Funding acquisition, Conceptualization. **Lucas A. Hof:** Writing – review & editing, Validation, Supervision, Resources, Project administration, Methodology, Funding acquisition, Conceptualization.

Declaration of competing interest

The authors declare that they have no know competing financial interests or personal relationships that could have appeared to influence the work reported in this paper.

Acknowledgments

Financial support from Mitacs (IT31045, IT39148, IT44408), VPM Research Inc., CRC Tier 1-2021-00489, and the Natural Sciences and Engineering Research Council of Canada (NSERC) under the Discovery Grant (RGPIN-2019-05973), is gratefully acknowledged. The help of Julie Valentin and Mathis Ginto (École de technologie supérieure, Montréal) in metal-polymer filaments extrusion, 3D printing and SEM analysis is also highly appreciated.

Data availability

Data used in the study can be made available by the authors upon request.

References

[1] Xue J, et al. Optimal process parameters for FDM-based 3D printing of metal-polymer mixtures with low-temperature powder feeding. Steel Res Int 2024;95(8):2300832.
[2] Miao X, Chin KC, Boydston AJ. Design, testing, and application of an open-source powder material extrusion 3D printer. Addit Manuf 2024;81:104014.
[3] Zerankeshi MM, Bakhshi R, Alizadeh R. Polymer/metal composite 3D porous bone tissue engineering scaffolds fabricated by additive manufacturing techniques: a review. Bioprinting 2022;25:e00191.
[4] Eyri B, et al. Characterization of ABS/PETG multi-material composites 3D printed by print-pause-print method. Polym Eng Sci 2025;65(5):2353–69.
[5] Wei X, Bähr R. A comparative study of 3D printing with virgin and recycled polylactic acid filaments. CIRP J Manuf Sci Technol 2024;54:75–84.
[6] Martins RF, et al. Mechanical properties of additively manufactured polymeric materials—PLA and PETG—for biomechanical applications. Polymers 2024;16(13):1868.
[7] Żur A, et al. Preliminary study on mechanical aspects of 3D-printed PLA-TPU composites. Materials 2022;15(7):2364.
[8] Masood S, Song W. Development of new metal/polymer materials for rapid tooling using fused deposition modelling. Mater Des 2004;25(7):587–94.
[9] Nikzad M, Masood SH, Sbarski I. Thermo-mechanical properties of a highly filled polymeric composites for fused deposition modeling. Mater Des 2011;32(6):3448–56.
[10] Kukla C, et al. Effect of particle size on the properties of highly-filled polymers for fused filament fabrication. In: AIP conference proceedings. AIP Publishing LLC; 2017.
[11] Ryder MA, et al. Fabrication and properties of novel polymer-metal composites using fused deposition modeling. Compos Sci Technol 2018;158:43–50.
[12] Thompson Y, et al. Fused filament fabrication, debinding and sintering as a low cost additive manufacturing method of 316L stainless steel. Addit Manuf 2019;30:100861.

[13] Hwang S, et al. Thermo-mechanical characterization of metal/polymer composite filaments and printing parameter study for fused deposition modeling in the 3D printing process. J Electron Mater 2015;44(3):771–7.
[14] Podsiadły B, et al. Electrically conductive acrylonitrile butadiene styrene (ABS)/copper composite filament for fused deposition modeling. In: Photonics applications in astronomy, communications, industry, and high-energy physics experiments 2018. International Society for Optics and Photonics; 2018.
[15] Hasib AG, et al. Rheology scaling of spherical metal powders dispersed in thermoplastics and its correlation to the extrudability of filaments for 3D printing. Addit Manuf 2021;41:101967.
[16] Wagner MA, et al. Fused filament fabrication of stainless steel structures-from binder development to sintered properties. Addit Manuf 2021:102472.
[17] Thompson Y, et al. Metal fused filament fabrication of the nickel-base superalloy IN 718. J Mater Sci 2022;57(21):9541–55.
[18] Gloeckle C, et al. Processing of highly filled polymer–metal feedstocks for fused filament fabrication and the production of metallic implants. Materials 2020;13(19):4413.
[19] Godec D, et al. Optimization of the 3D printing parameters for tensile properties of specimens produced by fused filament fabrication of 17-4PH stainless steel. Materials 2020;13(3):774.
[20] Nabipour M, Akhoundi B, Bagheri Saed A. Manufacturing of polymer/metal composites by fused deposition modeling process with polyethylene. J Appl Polym Sci 2020;137(21):48717.
[21] Tadi SP, Mamilla RS. Fabrication of SS 316L particle-infilled PLA composite filaments from cast-off bi-material extrudates for 3D printing applications. Waste Manag 2025;193:386–97.
[22] Karimi N, Fayazfar H. Development of highly filled nickel-polymer feedstock from recycled and biodegradable resources for low-cost material extrusion additive manufacturing of metals. J Manuf Process 2023;107:506–14.
[23] Tosto C, et al. Hybrid metal/polymer filaments for fused filament fabrication (FFF) to print metal parts. Appl Sci 2021;11(4):1444.
[24] Guerra MG, et al. Material extrusion-debinding-sintering as an emerging additive manufacturing process chain for metal/ceramic parts construction. In: CIRP novel topics in production engineering. Vol. 1. Springer; 2024. p. 147–82.
[25] Sadaf M, et al. Advancements in metal additive manufacturing: a comprehensive review of material extrusion with highly filled polymers. J Manuf Mater Process 2024;8(1):14.
[26] Eickhoff R, et al. Development of flexible and partly water-soluble binder systems for metal fused filament fabrication (MF3) of Ti-6Al-4V parts. Polymers 2024;16(17):2548.
[27] Cerejo F, Gatões D, Vieira M. Optimization of metallic powder filaments for additive manufacturing extrusion (MEX). Int J Adv Manuf Technol 2021;115(7):2449–64.
[28] Momeni V, et al. Binder system composition on the rheological and magnetic properties of Nd-Fe-B feedstocks for metal injection molding. Appl Sci 2024;14(13):5638.
[29] Rane K, Barriere T, Strano M. Role of elongational viscosity of feedstock in extrusion-based additive manufacturing of powder-binder mixtures. Int J Adv Manuf Technol 2020;107(11):4389–402.
[30] Kan X, et al. 316L FFF binder development and debinding optimization. Mater Res Express 2021;8(11):116515.
[31] Chang G, et al. Printing, debinding and sintering of 15-5PH stainless steel components by fused deposition modeling additive manufacturing. Materials 2023;16(19):6372.
[32] Silvain J-F, et al. Study on debinding and sintering conditions in extrusion-based additive manufacturing of 316L and 316L+ Cu. Metals 2023;13(11):1858.
[33] Kukla C, et al. Debinding behaviour of feedstock for material extrusion additive manufacturing of zirconia. Powder Metall 2019;62(3):196–204.
[34] Wei X, et al. Novel metal/biopolymer composite filaments for extrusion-based additive manufacturing using CuSn10 as example. Compos Part B Eng 2025;300:112468.
[35] Thompson Y, et al. Fused filament fabrication-based additive manufacturing of commercially pure titanium. Adv Eng Mater 2021;23(12):2100380.
[36] Tedla G, Rogers K. Characterization of 3D printing filaments containing metal additives and their particulate emissions. Sci Total Environ 2023;875:162648.
[37] Fontana L, et al. Evaluating self-produced PLA filament for sustainable 3D printing: mechanical properties and energy consumption compared to commercial alternatives. J Manuf Mater Process 2025;9(6):172.
[38] García Plaza E, et al. Analysis of PLA geometric properties processed by FFF additive manufacturing: effects of process parameters and plate-extruder precision motion. Polymers 2019;11(10):1581.
[39] Morettini G, et al. Comprehensive characterization of mechanical and physical properties of PLA structures printed by FFF-3D-printing process in different directions. Progress Addit Manuf 2022;7(5):1111–22.
[40] Reverte JM, et al. Mechanical and geometric performance of PLA-based polymer composites processed by the fused filament fabrication additive manufacturing technique. Materials 2020;13(8):1924.
[41] Akbar I, et al. Optimization of PLA/Mg/PEG biocomposite filaments for 3D-printed bone scaffolds using response surface methodology (RSM). Adv Manuf Polym Compos Sci 2025;11(1):2448648.
[42] Ranaiefar M, et al. Compressive properties of additively manufactured metal-reinforced PLA and ABS composites. Polymers 2024;16(14):2008.
[43] Shin EJ, et al. Eco-friendly TPU/PLA blends for application as shape-memory 3D printing filaments. J Polym Environ 2023;31(7):3182–96.
[44] Goh GD, et al. Exploring PLA/TPU blends in pellet-based printing for multifunctional applications: blending and interfacial properties. Mater Sci Eng R Rep 2025;164:100981.
[45] Masarra N-A, et al. Fabrication of PLA/PCL/graphene nanoplatelet (GNP) electrically conductive circuit using the fused filament fabrication (FFF) 3D printing technique. Materials 2022;15(3):762.
[46] Momeni V, et al. Effects of different polypropylene (PP)-backbones in aluminium feedstock for fused filament fabrication (FFF). Polymers 2023;15(14):3007.
[47] Tablit S, et al. Effect of chemical treatments of arundo donax L. fibre on mechanical and thermal properties of the PLA/PP blend composite filament for FDM 3D printing. J Mech Behav Biomed Mater 2024;152:106438.
[48] Harris M, et al. Partial polymer blend for fused filament fabrication with high thermal stability. Polymers 2021;13(19):3353.
[49] Austen W. The extraction of nickel from its ores by the mond process.(including plate at back of volume). In: Minutes of the proceedings of the institution of civil engineers. Thomas Telford-ICE Virtual Library; 1899.
[50] Singh, P., et al., Printability studies of Ti-6Al-4V by metal fused filament fabrication (MF3). Int J Refract Met Hard Mater, 2020. 91: p. 105249.
[51] Jacob J, et al. A review of fused filament fabrication of metal parts (metal FFF): current developments and future challenges. Technologies 2024;12(12):267.
[52] Sanetrnik D, et al. Effect of particle size and shape on wall slip of highly filled powder feedstocks for material extrusion and powder injection molding. 3D Print Addit Manuf 2023;10(2):236–44.
[53] Cabo Rios A, et al. Sintering anisotropy of binder jetted 316L stainless steel: part I–sintering anisotropy. Powder Metall 2022;65(4):273–82.
[54] Marczyk J, Hebda M. Effect of the particle size distribution of irregular Al powder on properties of parts for electronics fabricated by binder jetting. Electronics 2023;12(12):2733.
[55] Sadaf M, Bragaglia M, Nanni F. A simple route for additive manufacturing of 316L stainless steel via fused filament fabrication. J Manuf Process 2021;67:141–50.
[56] Jiang D, Ning F. Additive manufacturing of 316L stainless steel by a printing-debinding-sintering method: effects of microstructure on fatigue property. J Manuf Sci Eng 2021;143(9).
[57] Frunzaverde D, et al. The influence of the layer height and the filament color on the dimensional accuracy and the tensile strength of FDM-printed PLA specimens. Polymers 2023;15(10):2377.
[58] İncesu R, Akderya T. The influence of printing speed and temperature on the mechanical, absorptive, and morphological properties of PLA-based hybrid materials produced with an FDM-type 3D printer. Polymers 2024;16(19):2771.
[59] Beşliu-Băncescu I, Tamaşag I, Slătineanu L. Influence of 3D printing conditions on some physical–mechanical and technological properties of PCL wood-based polymer parts manufactured by FDM. Polymers 2023;15(10):2305.
[60] Lengauer W, et al. Fabrication and properties of extrusion-based 3D-printed hardmetal and cermet components. Int J Refract Met Hard Mater 2019;82:141–9.